ACS APPLIED NANO MATERIALS

www.acsanm.org

Article

# Optimization of Chromium-Doped Zinc Gallate Nanocrystals for Strong Near-Infrared Emission by Annealing

Mátyás M. Rudolf, Gábor Bortel, Bence G. Márkus, Nikoletta Jegenyes, Vladimir Verkhovlyuk, Katalin Kamarás, Ferenc Simon, Adam Gali,* and David Beke

Cite This: *ACS Appl. Nano Mater.* 2022, 5, 8950−8961

Read Online

ACCESS | Metrics & More | Article Recommendations | Supporting Information

**ABSTRACT:** Chromium-doped spinel crystals show long-lasting emissions in the near-infrared wavelength region. The emission can be activated by X-ray or ultraviolet−visible (UV−visible) light. Such properties make this material a promising candidate for background-free deep-tissue bioimaging, photodynamic or photon-induced therapy, and other applications. Here, we apply hydrothermal synthesis for the preparation of Cr-doped zinc gallate ($ZnGa_2O_4$) nanoparticles of small sizes with around 10 nm in diameter, which has the potential to be intravenously introduced to patients. We find that annealing of the as-prepared nanoparticles at 800 °C yields an order of magnitude increase in the emission intensity in the near-infrared wavelength region upon X-ray exposure with favorable long-lasting photoluminescence, which may be directly employed for deep-tissue cancer treatments when combined with IR700-mAb conjugate drug agents. We discuss the effect of annealing on the structural changes and the evolution of Cr defects of 10 nm Cr-doped zinc gallate nanoparticles by imaging techniques and monitoring their magneto-optical signals.

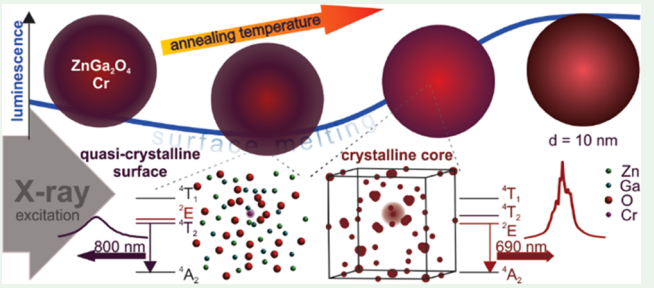


**KEYWORDS:** *zinc gallate, nanoparticle, annealing, chromium defect, XEOL, long-lasting photoluminescence, IR700 dye molecule, EPR*



## INTRODUCTION

Chromium-doped spinel crystals show strong, long-lasting emission in the near-infrared range[1] that can be activated even upon X-ray exposure, known as X-ray excited optical luminescence (XEOL) process. Such properties make this material a promising candidate for background-free bioimaging,[2−4] and, similarly to the family of doped spinel oxides,[5−8] these emitters may be used as a light source to trigger photodynamic or photoinduced therapy deep in the body, where these therapeutic approaches have not yet been accessible. A particular application of Cr-doped spinels can be the excitation of the IR700-mAb conjugate, a recently developed drug for photoimmunotherapy.[9,10] Indeed, both the X-ray excited infrared emission and the subsequent long-lasting luminescence of Cr-doped spinel nanocrystals have the potential for an effective IR700 excitation administered for deep-seated cancer treatment, which may replace invasive surgical interventions.

The infrared emission from Cr-doped $ZnGa_2O_4$ (ZGO:Cr) is due to the $^2E \rightarrow {}^4A_2$ transition of the Cr defect,[11] around 700 nm. However, the emission intensity, the long-lasting emission properties, and the spectral features are influenced by the crystal structure.[12] The zero-phonon R-line in the emission spectrum at around 688 nm originates from the perfect octahedral crystal orientation. The presence of neighboring defects (antisites or others) modifies the Cr defects' energy levels in different ways. First, the octahedral field strength variation shifts the $^2E \rightarrow {}^4A_2$ transition, resulting in new zero-phonon lines (N1, N2, etc.) aside from the R-line. Second, modification of the axial crystal field component and the appearance of a low-symmetry distortion modifies the splitting of $^2E$ and $^4A_2$ levels. In turn, the shape of the photoluminescence emission (PL) lines and the structure of the electron paramagnetic resonance (EPR) spectrum of the quartet ground state will also change. The nature of neighboring defects is likely to be responsible for the shallow and deep electron and hole traps indispensable for long-lasting photoluminescence (LLP).[13]

The conventional synthesis of spinel oxides with emission centers is annealing the mixture of particular oxides or hydroxides.[14−17] The solid-state reaction requires 800−1300 °C annealing temperatures. Treatment at such elevated temperatures leads to relatively large particle sizes with a broad size distribution. The defect concentration can be varied only through the variation of component ratio or by the

**Received:** March 16, 2022
**Accepted:** June 30, 2022
**Published:** July 12, 2022

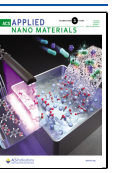

addition of other elements. On the other hand, the high synthesis temperature eliminates most of the defects and crystal imperfections. However, precise defect engineering is required for high emission intensity and bright LLP because these parameters depend on defect types and defect concentrations.

An emerging new synthesis route is solvothermal synthesis, i.e., the material is prepared from its soluble salts at high pressures and moderate (150−300 °C) temperatures.[18−21] Crystals grown this way can achieve nanoparticles (NPs) sub-10 nm particle size and narrow size distribution. On the other hand, the low reaction temperature and the arising reaction types can introduce defects and strain that influence the optical properties of the material. These defects and strain can have different temperature stability from the previously identified defects. Low temperature (below 600 °C) stability is important for thermometric[22] or thermoluminescence applications, while higher temperatures tend to change the optical properties.

The temperature dependency of these defects has not yet been investigated because the majority of ZGO:Cr was prepared by a solid-state reaction at a high reaction temperature. Despite the good optical properties of the hydrothermally synthesized ZGO:Cr nanoparticles, an enormous effort has been made to further improve the optical properties. The concentration of the Cr defect[23,24] and the presence of other dopants[25−27] play a critical role in the optical properties. Annealing is also a popular method to improve the physical, more specifically, the optical properties of doped ZGO NPs. It is reported that the annealing of ZGO at 800 °C[28] or ZGO:Cr at 750 °C[18] increases the crystallinity and the crystallite size. A 6-fold increase in the intensity of the photoexcited emission was also observed. Annealing ZGO:Cr, Bi−$SiO_2$ core−shell particles at 1000 °C also increased the emission intensity without a significant increase in the particle size.[27] Zou studied the persistent luminescence properties of silica-coated ZGO:Cr NPs as a function of annealing temperature and time.[29] They achieved the best performance in LLP at 900−1000 °C annealing without significantly increasing the 15 nm particle size. In contrast, in ZGO:Cr NPs synthesized via the citric acid-assisted sol−gel method, a gradual increase in both the NP size and the emission intensity was found with annealing.[30]

In our previous study, the hydrothermal method was applied for synthesizing ZGO:Cr NPs using silicon carbide (SiC) NPs seed.[24] We found an efficient energy transfer from SiC NPs toward ZGO:Cr NPs, which enhanced the emission by an order of magnitude. We also optimized the concentration of Cr in ZGO:Cr NPs for maximum emission in that study.[24] On the other hand, the synthesis of the complex multiparticle system could limit the applicability and make it difficult to develop robust technology for preparing the material in macroscopic amounts.

Here, our aim is to develop such ZGO:Cr NPs that possess advanced emission properties upon X-ray exposure without the need for seed in the synthesis process. Our idea is to focus on the defect engineering of the host ZGO NPs, which can be principally carried out by well-designed annealing strategies as previous studies cited above imply already. Therefore, we use the hydrothermal method to synthesize ZGO:Cr NPs with optimized Cr concentration[24] and anneal these NPs at different temperatures ($T_A$) between 200 and 1100 °C to find the best condition for maximizing the emission intensity and LLP upon X-ray exposure. While previous studies focused on the optimization of a selected property (i.e., emission intensity upon ultraviolet (UV) illumination or, more frequently, the LLP time), we are focusing on the understanding of the changes in the material that results in changes in the optical properties. Some of the ZGO:Cr NPs, therefore, are covered with silica shells using standard Stöber silica synthesis before annealing (see the Methods section), to understand the effect of surface types and size of the NPs in the process. The stability of the defects present after the synthesis is analyzed. The changes in the physical and magneto-optical properties achieved by different annealing treatments are studied by various techniques to find the correlation between the structural changes in the ZGO:Cr NPs such as the size, the crystallinity of the host material, as well as the defect concentration and the intensity of emission and LLP time upon ultraviolet (UV) and X-ray exposure. UV exposure is applied to understand the mechanism of excitation of ZGO:Cr color centers. We quantify the excitation probability of IR700 probes by X-ray exposure of our ZGO:Cr NPs toward the application of combined ZGO:Cr NPs and IR700-mAb conjugate drug agents for deep-tissue cancer treatments.

## RESULTS

We prepared various ZGO:Cr samples using annealing temperatures to control the size, crystallinity, and defect concentrations with or without silica coating as described in the Methods section. Silica-coated samples labeled as ZGO:Cr−$SiO_2$. Afterward, we analyzed their emission intensity and LLP performances (cf., Figures 1 and 2) upon

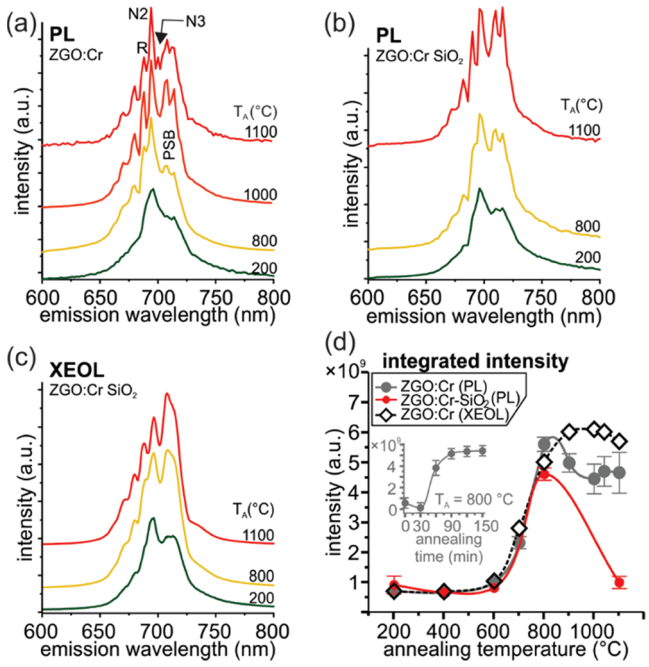


**Figure 1.** Room-temperature photoluminescence emission spectra of (a) ZGO:Cr and (b) ZGO:Cr−$SiO_2$ NPs. The emission changes with annealing temperature ($T_A$). (c) Room-temperature XEOL spectrum as a function of $T_A$ for ZGO:Cr−$SiO_2$ samples. Emission spectra are normalized and vertically shifted for the sake of visibility. (d) Integrated emission intensities as a function of $T_A$ or annealing time (inset) were calculated by integrating the spectra between 650 and 750 nm. Annealing-time optimization was carried out at $T_A$ = 800 °C. Error bars are presented for the samples and repeated measurements for which the deviation exceeds 1%.



https://doi.org/10.1021/acsanm.2c01156
ACS Appl. Nano Mater. 2022, 5, 8950−8961

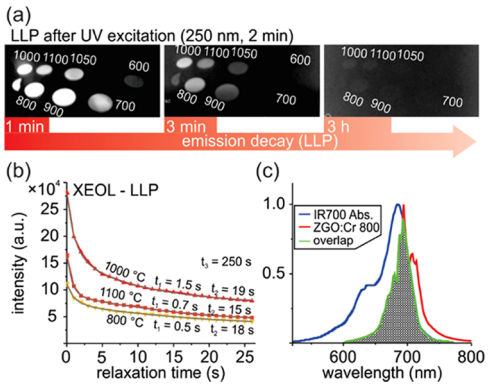


**Figure 2.** (a) Long-lasting luminescence of ZGO:Cr samples after 2 min of 250 nm excitation as recorded by the camera and (b) the decay curve of the emission after X-ray excitation derived from the recorded data of the spectrometer. The labels in (a) refer to the annealing temperature in Celsius degrees of the ZGO:Cr samples. The decay curve is calculated by integrating the emission spectra between 650 and 750 nm at each measurement time. (c) Overlap between the emission spectrum (ZGO:Cr-800) and the absorption spectrum of IR700 dye.

UV or X-ray irradiation. The applied $T_A$ is indicated at the end of the sample names, e.g., ZGO:Cr-600 label means that the ZGO:Cr sample was annealed at 600 °C. While the outcome of the PL intensity and LLP time give the information for the optimal annealing temperature and time, we carried out additional characterization and analyzed the data together to unravel the structural changes leading to the $T_A$-dependent PL intensity and LLP, and the different response to X-ray and UV excitation.

The ZGO:Cr samples show PL intensity increase and peak narrowing at elevated $T_A$ regardless of the surface, but the enhancement in the emission intensity is not monotonous with $T_A$. The highest emission intensity upon UV excitation was reached for samples that were annealed at 800 °C, with a decrease in the PL intensity and an increased standard deviation for samples with $T_A$ > 900 °C. The zero-phonon line (ZPL) peaks become distinguishable at $T_A$ = 600 °C. The N2 line dominates the emission at room temperature, and only the R lines, as one peak, and the N2 line can be identified beside the phonon sidebands. The only exception is for samples with $T_A$ = 1100 °C, for which the presence of the N3 type defect is also detectable. Interestingly, the intensities decreased for samples with $T_A$ = 200−600 °C.

XEOL shows a similar behavior in the emission intensity as a function of $T_A$. However, the maximum emission intensity is shifted to $T_A$ = 900−1000 °C, and the decrease has a slighter slope compared to those of UV illumination. This suggests a different decay mechanism for the two processes. The peak profile of XEOL changes in a similar manner to that observed by PL. The different line shape of luminescence is due to the lower resolution of the spectrometer used for XEOL than that for PL. We employed 2 and 10 h annealing times, and we see no differences in the observed properties. The optimization of the annealing time was carried out at $T_A$ = 800 °C. After 30 min, the PL intensity dropped and then increased and reached the maximum over 2 h.

Figure 1 shows the corresponding emission spectra (Figure 1a−c) of ZGO:Cr and ZGO:Cr−$SiO_2$ samples at $T_A$ where significant spectral changes happened, together with the changes in the intensity as a function of $T_A$ (Figure 1d) or time (inset in Figure 1d). Emission intensity is calculated by integrating the PL and XEOL spectra between 650 and 750 nm.

Besides the emission intensity during continuous excitation, the LLP properties of this material are considered essential for various applications. LLP was studied under three different excitation wavelengths: 365, 250 nm, and X-ray (see the Methods section).

In most studies, LLP is measured with a night vision camera, and LLP time is defined as the duration for which the camera can detect the emission from the material after switching off the excitation source.[31] This definition, however, cannot be accurate because, in that case, LLP time depends on the overall sensitivity of the setup (camera sensitivity, which is affected by other optical elements, sample size, and sample distance). We studied the LLP with a camera without infrared (IR) filter and a spectrometer to derive the time constants and the absolute irradiance from the recorded PL spectrum. We use the latter method for quantitative comparison of different samples, whereas the former method is applied for illustration of the process (e.g., Figure 2a).

The LLP properties were significantly increased in samples annealed above $T_A$ = 600 °C. The longest LLP was measured after 2 min of 250 nm excitation, 6 h. 365 nm excitation resulted in about 4 h of LLP, while the shortest LLP was measured under X-ray excitation (2.5 h). Under X-ray excitation, $SiO_2$-covered and bare ZGO:Cr NPs show LLP emission, which correlates with the measured intensity during continuous X-ray excitation. Namely, samples annealed at 800 and 900 °C showed the brightest emission and the longest decay time for $SiO_2$-covered and bare ZGO:Cr NPs, respectively.

In contrast, ZGO:Cr-1000 NPs are the brightest right after the excitation was switched off when UV excitation was used. However, the measured LLP time was almost the same as for samples treated with $T_A$ = 800−1100 °C. The emission intensity of the ZGO:Cr-1000 NPs decreased to the level of the other samples within 15 min upon 250 nm excitation.

The emission peak was integrated after X-ray excitation to calculate the relaxation time. Two exponentials are required, to fit the early evolution of relaxation. Figure 2 shows the camera images at different times recorded after 2 min upon 250 nm exposure and the decay curves for the best three samples.

We quantified the brightness as absolute irradiance, that is, the energy density coming from the samples, and it is used to quantify the dose of the light used in photoinduced therapy. The absolute irradiance was calculated for the ZGO:Cr-900 samples' integrated peak area using the XEOL setup geometry. This calculation results in a 1.4 mW/cm$^2$ total photon flux from the sample under continuous X-ray excitation after saturation in XEOL intensity has been reached. We note again that the saturated XEOL intensity drops, in our case, to 70 $\mu$W/cm$^2$ within 10 s after the X-ray excitation was turned off, and it decreases further exponentially with the previously given long lifetime in Figure 2b.

The measured irradiance under continuous X-ray excitation is about 10 times lower than the 12 mW/cm$^2$ minimum power density used in previous phototherapy applications.[9,10] The minimum effective dose for IR700 activation[32] is 2 J/cm$^2$. We calculated the time required for the effective dose by determining the overlap integral between the absorption of IR700 dye and the emission of ZGO:Cr-800 and ZGO:Cr-1100 samples, and those are 63 and 51%, respectively. These


https://doi.org/10.1021/acsanm.2c01156
ACS Appl. Nano Mater. 2022, 5, 8950−8961

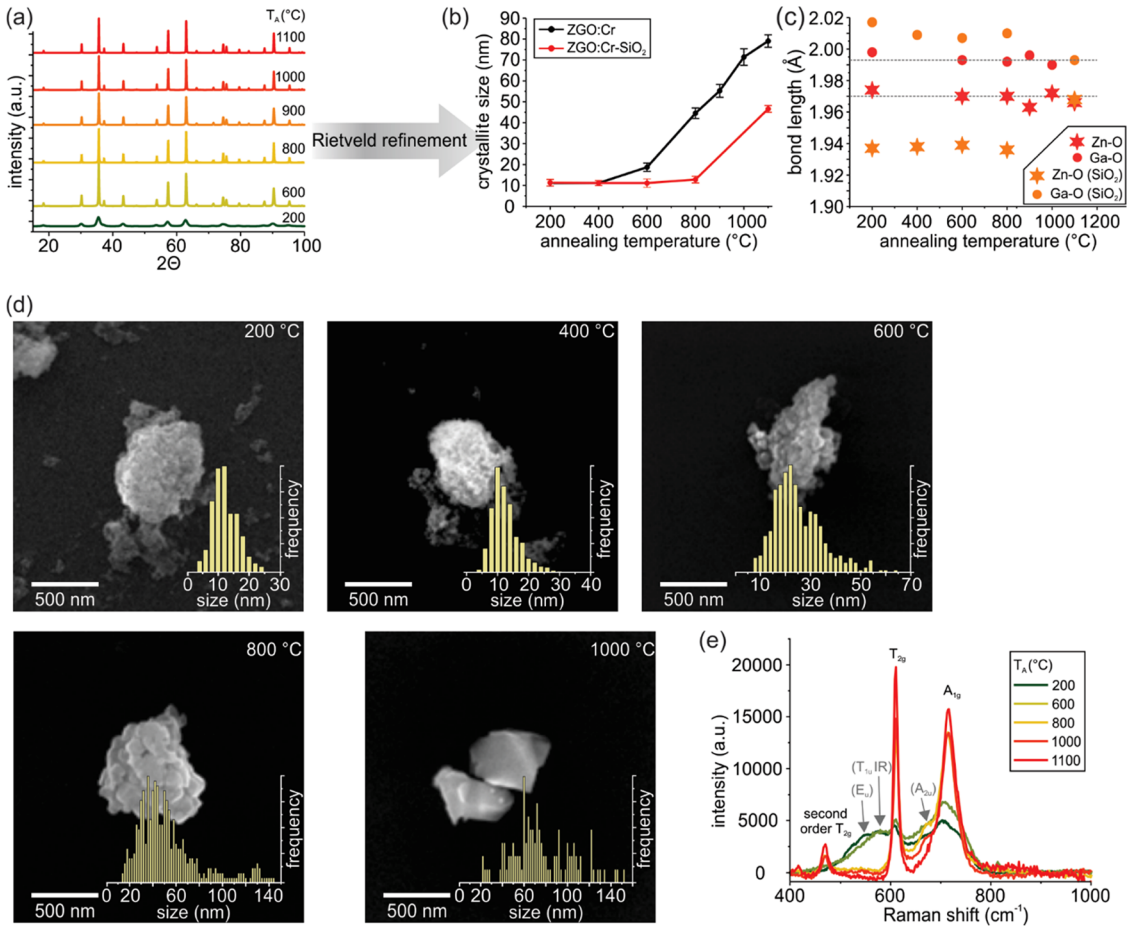


**Figure 3.** (a) XRD data of ZGO:Cr, and (b) the calculated crystal sizes and (c) bond lengths obtained from Rietveld analysis. Error bars for crystallite size represented the variation in the particle size in the repeated experiments in (b). The reference values for Ga−O (top) and Zn−O (bottom) bond lengths are plotted as horizontal dotted gray lines in (c). (d) Scanning electron microscopy (SEM) image of ZGO:Cr aggregates and particle size distribution and (e) Raman spectra of ZGO:Cr as a function of annealing temperature. Raman active peaks are labeled in black. Non-Raman-active peak positions are labeled in gray when they coincide with a measured peak maximum.

values give 35 and 45 min of treatment time under continuous excitation for ZGO:Cr-900 and ZGO:Cr-1100 samples, respectively. Moreover, 12 or 18 h LLP times are approximately equivalent with 2 J/cm$^2$ doses, again, for ZGO:Cr-900 and ZGO:Cr-1100, respectively. The results are very conservative estimates because not all of the emitted light was collected in the measurements (see Methods). We conclude from the calculation that our developed chromium-doped ZGO NPs are directly applicable photodynamic or photothermal therapy under soft X-ray exposure for activation of IR700-mAb drug anticancer agents.[9,10]

Although an appropriate camera is suitable to measure LLP, rather decay time and absolute irradiance elaborate the process for different types of application. The calculated dose as a function of time provides a measure, i.e., for photon-induced and photothermal therapies, and the intensity decay itself is suitable to compare and select samples for other applications, i.e., LLP tagging. Our annealing studies show that ZGO:Cr NPs change continuously as a function of $T_A$ and such changes significantly affect the emission properties. Emission intensity goes over a maximum that depends on the excitation energy. LLP is considerable only over 600 °C $T_A$, and the LLP time also depends on $T_A$ and the excitation energy. Further optimization promises improved performance for the desired application (i.e., high emission intensity under excitation and designed LLP time and intensity decay), but requires a deep understanding of the underlying structural changes and defect creation upon annealing. In addition, the magneto-optical and other properties of the defects and the host nanoparticle should be well understood as we discuss below.

## DISCUSSION

The luminescence measurements revealed that the annealing of ZGO:Cr NPs after hydrothermal synthesis can significantly improve certain optical properties. The brightest emission can be achieved when $T_A$ at 800−900 °C is applied. On the other hand, the photoluminescence study shows that some physical or chemical processes are also generated during annealing. The emission intensity upon UV illumination decreased for $T_A$ = 400−600 °C and $T_A$ > 900 °C despite the more pronounced ZPL lines of Cr defects at higher annealing temperatures which are the indicators of improved crystalline quality.

The X-ray diffraction (XRD) data show the pure $ZnGa_2O_4$ phase for all samples (Figure 3a). There is no sign of peak shift due to stress relaxation. We calculated the crystallite size (Figure 3b) and the bond distances (Figure 3c) from the diffractogram. The crystallite size gradually increases with the annealing temperature for ZGO:Cr, and there is no increase for $T_A$ < 800 °C for ZGO:Cr−$SiO_2$. There is a slight decrease in the Zn−O and the Ga−O bond lengths for ZGO:Cr


https://doi.org/10.1021/acsanm.2c01156
ACS Appl. Nano Mater. 2022, 5, 8950−8961

samples, but overall, the variation in the lattice parameters is below the margin of error, and the calculated bond lengths are in agreement with the reported values in the literature,[33] implying that the ZGO:Cr nanocrystals are well crystallized right after the hydrothermal reaction and no global disorder develops according to the X-ray diffractogram. The bond lengths calculated for ZGO:Cr−$SiO_2$ NPs show a higher deviation that can be explained by the presence of $SiO_2$, and the presence of Si−O−M bonds on the surface, where M indicates metallic ions.

Scanning electron microscopy (SEM) images (Figure 3d) revealed the increase of the ZGO:Cr particle size and the smoothening of the surfaces with increasing $T_A$. Particle size distribution was calculated by measuring the particle size on several SEM images. The calculated size distributions have a mode value close to the crystallite size calculated from X-ray diffractograms. SEM images taken on the ZGO:Cr−$SiO_2$ samples reveal the presence of spherical $SiO_2$ particles with an average diameter of 70 nm and small particles with a diameter of about 15 nm (Figure S1). Electron diffraction spectroscopy (EDS) shows uniform ZGO:Cr distribution. The ZGO:Cr particle size was measured after silica was removed by HF etching (Figure S2). The particle size of the ZGO:Cr−$SiO_2$ samples by SEM correlates well with the crystallite size calculated from the XRD data.

From the XRD and the SEM data analysis, it can be concluded, that the ZGO:Cr particles are dominated by monocrystals. Particle size is increasing with $T_A$ without the presence of $SiO_2$. Silica can prevent Oswald ripening, and other processes cause an increase in the particle size at $T_A$ < 800 °C. However, ZGO:Cr NPs start to grow even when a $SiO_2$ coverage is present provided that the annealing temperature reaches 800 °C. SEM images reveal that the surface of the aggregates starts to become smooth at $T_A$ = 600 °C (ZGC:Cr-600). These observations are signs of extended diffusion ability of the components for $T_A$ > 600 °C. The particle growth of ZGO:Cr−$SiO_2$ shows that the components can move through the porous $SiO_2$ matrix that cannot prevent Oswald ripening. Indeed, annealing affects both the ZGO:Cr and the silica NPs. The latter suffers from pore shrinkage at $T_A$ > 600 °C that can result in a complete loss of porosity at around 1100 °C.[34] The large deviations in bond lengths in ZGO:Cr−$SiO_2$ samples for $T_A$ < 800 °C indicate that the surface influences the overall properties, especially, for particle sizes below 40 nm in diameter. Indeed, the percentage of the atoms at the surface in a 10 nm particle is about 40%, while it is less than 5% for a 40 nm particle.

Raman spectroscopy also shows an increase in the crystalline quality for samples annealed at certain temperatures (Figure 3e). Raman spectra show the evolution of the two Raman active modes, $T_{2g}$ and $A_{1g}$. The sharp second-order peak at 467 nm can be observed for samples with $T_A$ > 800 °C. The Raman active modes become more dominant and narrower with the increase of $T_A$. For samples with $T_A$ < 800 °C, the $A_{1g}$ peak is a doublet, and for ZGO:Cr-200 and -400 samples, other peaks can be also detected. These smaller features resemble sidebands of other modes. The peak positions, however, match the non-Raman-active resonant frequencies. The reduced symmetry from low-quality crystal often results in more optical and vibrational transitions because of the relaxed selection rules valid for the perfect crystalline environment, i.e., "forbidden transitions", thus the optical spectra could be a measure of the quality of the crystal. Indeed, the Raman active peaks become narrower with elevated annealing temperatures, and the intensity of the otherwise forbidden modes decreases at $T_A$ = 800 °C. The same holds for the ZGO:Cr−$SiO_2$ samples showing a temperature-dependent rather than size-dependent decrease of the disorder that modifies the selection rules and broadens the Raman spectra as plotted in Figure S3.

XRD and Raman studies yield information about the ZGO crystal matrix. These results show a significant increase in the "quality" of the overall crystal structure for $T_A$ of 600 and 800 °C. SEM also shows a significant decrease in the surface roughness when aggregates are studied. These observations and the particle size growth of the ZGO:Cr−$SiO_2$-800 sample suggest component diffusion, which starts or significantly increases for $T_A$ = 600−800 °C. However, the crystal structure and particle size modifications cannot fully explain the observations in the optical properties by varying the $T_A$ as the emission intensity decreases for $T_A$ > 900 °C with improved crystallinity regardless of the crystallite size, and even an annealing temperature as low as 400 °C can affect the optical properties. Therefore, the properties of the local environment around the Cr defects are also studied with EPR, low-temperature PL (LTPL), and photoluminescence excitation (PLE) spectroscopy.

Although the LTPL spectra are too broad for samples with $T_A$ < 600 °C to identify all of the different local distortions, the ZPLs are narrow for samples treated at a higher $T_A$ for identifying the defect centers. Table 1 contains the peak positions and the notations from ref 35

LTPL data shows that both size and $T_A$ modify the contribution of the different Cr defects to the optical signals. By elevating the annealing temperature, the FWHM of the ZPLs (Figure 4a,b) shrinks and the EPR spectra becomes also narrower (Figure 5a,b), implying a gradual improvement in the

**Table 1. Zero-Phonon-Line (ZPL) Positions in the Photoluminescence and Absorption Spectra**[a]

| | ZPL position (accuracy: 0.2 nm) | | | observation |
|---|---|---|---|---|
| label | (nm) | $cm^{-1}$ | eV | (low → high intensity) |
| R2 | 685.6 | 14585.7 | 1.808 | 1100, 1000, 800, 900, |
| R1 | 687.1 (690) | 14553.9 | 1.804 | 200 → 1100 |
| N1 | 689.4 | 14505.3 | 1.798 | 800 → 1100 |
| N1 | 690.2 | 14488.5 | 1.796 | 600 → 1100 |
| N2 | 693.3−694.0 | 14423.7−14409.2 | 1.879 | 200, 400 broad, 600, 1100, 1000, 900, 800 |
| N2 | 695.5 (695.9) | 14378.1 | 1.782 | 1100 → 800 |
| N2 | 697.2 | 14343.1 | 1.778 | 600 |
| N2 | 697.8 | 14330.7 | 1.777 | 600 → 900 |
| N2 | 699.2 | 14302.1 | 1.773 | 800, 900 |
| N3 | 700.0 | 14285.7 | 1.771 | 1000, 1100 |
| N3 | 702.5 | 14234.9 | 1.765 | 1000, 1100 |
| N5 | 718.9 | 13910.1 | 1.7 | 1000, 1100 |
| N5 | 720.7 | 13875.4 | 1.72 | 1000, 1100 |
| N6 | 729.8 | 13702.4 | 1.70 | 1000, 1100 |
| N7 | 735.2 | 13601.7 | 1.69 | 1000, 1100 |

[a]For a given center, the ZPL may shift depending on the environment; therefore, multiple ZPL positions may be associated with it. The "Observation" column shows the applied annealing temperatures in Celsius degrees before the observation of the optical spectrum.



https://doi.org/10.1021/acsanm.2c01156
ACS Appl. Nano Mater. 2022, 5, 8950−8961

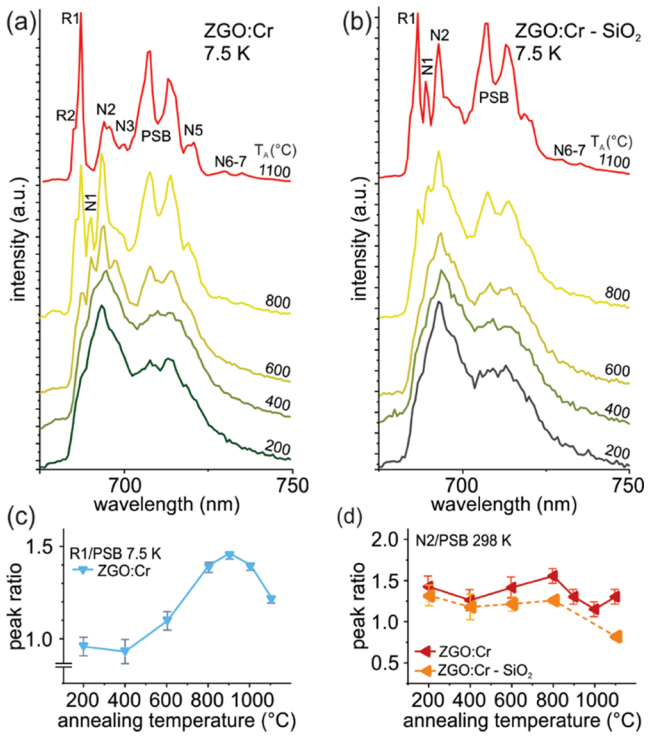


**Figure 4.** Low-temperature PL (LTPL) spectra of (a) ZGO:Cr and (b) ZGO:Cr−$SiO_2$. Calculated peak ratios from (c) LTPL spectra and (d) room-temperature PL. Spectra were normalized and shifted vertically for better visibility. The R1/PSB LTPL intensity ratio (c) correlates with the emission intensity upon X-ray excitation, while (d) the N2/PSB PL intensity ratio at room temperature correlates with the emission intensity upon UV excitation. Error bars represent the variation in the calculated ratios for the repeated samples and the calculated error for the deconvolution of the PL and LTPL spectra.

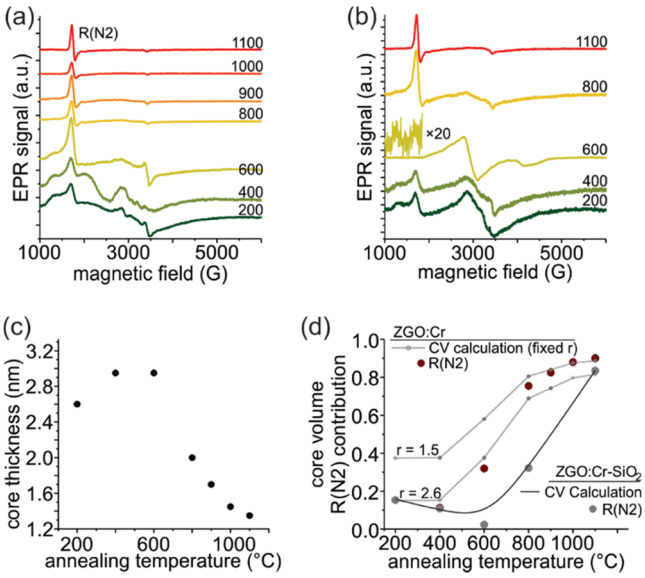


**Figure 5.** (a) EPR spectra of ZGO:Cr and (b) ZGO:Cr−$SiO_2$ samples at different annealing temperatures. Spectra were vertically shifted for better clarity. Intensity is not normalized. The same amount of sample measured makes the measured intensities comparable. (c) Equation 1 is used to fit the R(N2) contribution to calculate the diameter of the perturbed core volume (CV). (d) Calculated contribution of the R(N2) signal to the total EPR signal for the samples. These values were used to calculate CV as a function of size for ZGO:Cr−$SiO_2$ and compared to the R(N2) ratio.

local order around the Cr defects, which correlate well with XRD and Raman results. LTPL also shows a decrease in the contribution of the N2 line and an increase of R1 and R2 lines which becomes intense at $T_A$ > 800 °C. On the other hand, N1 and N3 centers' concentrations correlate with the crystallite size instead of $T_A$. Indeed, the crystallite size of ZGO:Cr-800 and ZGO:Cr−$SiO_2$-1100 are comparable. The same holds for the N1 and N3 centers' concentrations, while R1 and R2 centers become dominant for ZGO:Cr−$SiO_2$-1100. It is also observed that defect concentrations depend on the annealing temperature but not the annealing time, if the annealing time is long enough (2 h) for the equilibrium which suggests that all of the observed defects are stable at the studied temperature range. Temperature increase introduces global reorientation in the spinel host that affect the Cr environment, therefore the defect types and their relative concentrations at a certain temperature. This is also manifested in the temperature dependence of the Raman signals.

The contribution of the different Cr defects affects the overall luminescence intensity because they have different excitation and relaxation probability. However, the observed emission varies for UV- and X-ray excitation and for the LLP. The $^2E-^4A_2$ optical transition is spin-forbidden which may be allowed by spin-orbit mixing of doublet and quartet states mediated by phonons, appearing as a broad feature in the PL spectrum, called phonon sideband (PSB), in a perfect crystalline environment. On the contrary, the N2 center is expected to show a strong emission since the symmetry of the crystal field is distorted by proximate antisite defects. The increase of the R1 and R2 centers' contributions to the luminescence decreases the overall PL intensity due to the low quantum yield of the spin-forbidden transitions. On the other hand, the N2 center is always dominant at room temperature. The difference between the LTPL and the room-temperature PL spectra suggests an energy transfer from the R1 center to the N2 center, which is frozen or restricted at low temperatures. Indeed, while the LTPL spectrum of ZGO:Cr−$SiO_2$-1100 shows similar peak ratios to ZGO:Cr-800, the room-temperature PL spectrum features a sharp R1 line, indicating a high R1 center's concentration and restricted energy transfer.

Despite the complex defect structure and energy transfers in the development of the final optical signals of Cr-doped ZGO NPs, the emission intensity upon continuous illumination may be determined by the overall nature of the optical transition. Optical centers with "forbidden" optical transitions generally possess a large PSB in the PL spectrum. We plotted the ratio between PL intensities of N2 center and PSB features recorded at 298 K in Figure 4d. The trend in the N2/PSB PL intensities ratio is very similar to the emission plots of the UV excited spectra (cf. Figure 1d). The decrease in the contribution of the N2 center to the emission explains the drop in the overall PL intensity for samples with $T_A$ > 800 °C. The appearance of the R1 center at room temperature suggests that the increase of the R1 center's concentration relative to N2 center's concentration decreases the efficiency of the energy transfer that results in a decrease of the quantum yield due to the forbidden transition for the R1 center. It can be also concluded that while the concentration of the Cr defects correlates with particle size, the energy transfer's efficiency correlates with $T_A$.



https://doi.org/10.1021/acsanm.2c01156
ACS Appl. Nano Mater. 2022, 5, 8950−8961

The emission intensity under X-ray excitation has a different $T_A$ dependence. The main difference between the UV excitation and X-ray photons is that the former produces only electronic transitions associated with the Cr centers while the latter can excite deep core electrons to the conduction band. Therefore, the recovery to the ground state follows quite different routes in the two methods. The PSB is more dominant under X-ray excitation and even the anti-Stokes PSB is visible in some cases with a slightly higher R1−R2 centers' contribution than that upon UV excitation (see Figures S4 and S5). For samples with $T_A$ > 600 °C, PSB is the most intense feature during continuous X-ray excitation. The high-intensity emission of the N2 center regardless of the employed $T_A$ shows that the energy transfer between R1 and N2 defects still contributes to the relaxation process, but the cascade relaxation induced by the high-energy X-ray photon favors the R1/R2 defects in well-crystallized matrix. Indeed, the R1/PSB PL intensity ratio at 7.5 K has a trend similar to the XEOL intensity as a function of $T_A$.

While the N2 PL center has an increased brightness due to its intrinsically large optical dipole moment compared to that of the R1 center, LLP is more likely associated with the electron and hole transfer from deep traps toward N2 defects. The shortest LLP time upon X-ray excitation and the longest LLP time upon 250 nm excitation indicate that many trap states are dark states with ground states' levels close to the level of $^4A_2$ ground state and excited states' levels close to the level of one of the excited states, e.g., the $^4T_1$ state, of the Cr defect. Trap concentration and position of the levels of the traps determine the LLP decay and they are relatively independent of Cr defect but obviously depend on the crystal structure. Without annealing the hydrothermally synthesized NPs, the LLP is very short (min). EPR and Raman data show the annihilation of local imperfections and reduction of the intrinsic defect concentration in the ZGO crystal which reduces the exciton annihilation paths and channels excitons to various Cr defects with increasing the LLP time. As was shown previously, when the excitation is turned off, both the R1 and PSB PL intensities drop, and the dominant emission comes from N2 center during LLP. If the relaxation from the electron and hole traps only occurs via the N2 defect then the LLP time or, at least, the PL intensity at the early stage, would decrease with a lower concentration of N2 center. However, LLP is bright at the beginning of the process for the ZGO:Cr-1000 sample for which the N2 center's concentration is significantly lower than that in ZGO:Cr-800 and -900 samples. The dominance of the N2 center during LLP can be explained by the proposed energy transfer. Because the Cr defect concentration is constant in the samples, only the relative concentration of the different Cr defect types changes. LLP mostly depends on the concentration and the position of the exciton traps and does not drop with the decrease of the N2 center's concentration, thus N2 center is not associated with the defect responsible for the LLP process in ZGO:Cr, in contrast to previous suggestions in the literature.[36,37] The N3 concentration increases for $T_A$ > 800 °C according to the LTPL spectra, but this emission band is only visible for the ZGO:Cr-1100 and ZGO:Cr−$SiO_2$-1100 samples at room temperature. It is reported that N3 is a Cr−Cr pair defect and has different ground state's level position than that of N2 and R1 centers. The absence of the N3 emission at room temperature is due to an energy transfer from the Cr−Cr pair defects to single Cr defects.[35] The appearance of the N3 center at $T_A$ = 1100 °C explains the different decay curves at the beginning of the LLP. N3 center's concentration and the higher ground state's level of the N3 defect with respect to that of N2 and R1 centers leads to faster recombination from the trap states.[35] It should be noted that high-temperature annealing also induces Zn diffusion that can create new trap states and ZnO phase formation. We do not observe new phase formation in either the X-ray diffractograms or the Raman spectra, nevertheless, Zn interstitials might appear at high-temperature annealing of ZGO.

The EPR spectra (Figure 5a,b) show a characteristic peak of the unperturbed Cr in ZGO at around 1500 G. We use R(N2) notation for this peak, as it has exactly the same origin as the ZPLs in the photoluminescence spectra noted as R1, R2, and N2. These belong to unperturbed, slightly perturbed Cr centers and the Cr centers with neighboring antisite defects, respectively. Besides the R(N2) line, a complex, broad feature assembled from multiple peaks of the differently perturbed Cr defects can be observed. Broad Cr EPR lines in the ZGO matrix are explained by the enormous E and D zero-field-splitting parameters induced by strain which is connected to the variance in the Cr−O and M−O bond lengths close to the Cr defect.[13,38] By increasing the annealing temperature, the R(N2) peak increases while the broad peak decreases regardless of the presence of the $SiO_2$ shell. However, the EPR spectra of ZGO:Cr−$SiO_2$-800 and ZGO:Cr−$SiO_2$-1100 samples are closest to the EPR spectra of ZGO:Cr-600 and ZGO:Cr-800 samples, respectively. Indeed, the particle sizes are similar for the two sets of samples at different $T_A$ due to the restricted particle growth for $SiO_2$-covered samples that suggest a correlation between the measured EPR signals and the particle size.

We plotted the contribution of the EPR R(N2) line as a function of annealing temperature calculated from the integrated area of the R(N2) line and the whole spectrum (Figure 5d). The graph shows a sigmoidal correlation with a significant decrease at $T_A$ = 400 °C and $T_A$ = 400−600 °C for ZGO:Cr and ZGO:Cr−$SiO_2$ samples, respectively. While the increase of the crystallite size with $T_A$ is not sigmoidal (see Figure 3b), the surface-to-volume ratio is. For NPs, a significant number of unit cells is located near the surface. Surface unit cells have dangling bonds and surface-related chemical structures, i.e., −OH and adsorbed or chemisorbed water. Therefore, chromium defects close to the surface reside in various nonequivalent environments, manifested in the PL and EPR spectra as broadening of the bands or as an appearance of new bands. The influence of the surface chemistry around 10 nm particle size is visible in the changes of the M−O bond lengths after $SiO_2$ surface modification (see Figure 3c). If we assume that Cr defects are homogeneously distributed inside the NPs, the concentration of the Cr in a highly disturbed near-surface environment is proportional to the volume of this layer relative to the perfect crystalline core. The volume of the shell can be calculated by the following formula

$$V_s = \frac{4\pi}{3}R_t^3 - \left(\frac{4\pi}{3}(R_t - r)^3\right) \quad (1)$$

where $R_t$ is the radius of the ZGO:Cr NPs and $r$ is the thickness of the near-surface volume. With a constant $r$ for all $T_A$, the best fit gives 2.26 nm thickness for the shell at low $T_A$ and 1.50 nm for high $T_A$. The lower value is still twice the size of the 0.83 nm unit cell parameter of ZGO, implying that if the


https://doi.org/10.1021/acsanm.2c01156
ACS Appl. Nano Mater. 2022, 5, 8950−8961

recorded effect is surface-related, then it exceeds a single unit cell and changes with $T_A$.

Based on this assumption, we allowed the variation of $r$ to fit the R(N2) contribution in the EPR spectra of the ZGO:Cr sample. The calculated values are plotted in Figure 5c. These values are used to fit the R(N2) contribution of ZGO:Cr−$SiO_2$ samples (Figure 5d). The deviation is the most pronounced for ZGO:Cr-600 samples.

The fitted core thickness has a maximum at $T_A$ = 400−600 °C with a rapid exponential decay at higher temperatures. The LTPL spectra of the samples annealed at 400 and 600 °C also differ from the other spectra (Figure 4c). The spectrum has a very long tail in the near-infrared region. The deconvolution of the LTPL spectra shows a relatively broad emission among the ZPL lines, at 735 nm (1.69 eV) at low $T_A$ corresponding to the unresolved N6 and N7 centers. The energy levels of the Cr defects strongly depend on the crystal field strength. At a low crystal field strength, the emission is coming from the $^4T_2$−$^4A_2$ transition. This emission is weak and red-shifted compared to the $^2E$−$^4A_2$ transition at a high crystal field strength.[39−41] The crystal field strength is small in amorphous ZGO, and because of that, the Cr-related $^4T_2$−$^4A_2$ transition emission is highly red-shifted. The average crystal field strength can be estimated from the photoluminescence excitation (PLE) spectrum. A redshift in the $^4T_2$−$^4A_2$ and $^4T_1$−$^4A_2$ transitions verifies the reduced crystal field strength.[13,23] The fitted and calculated values can be found in Table 2, where the numbers in the brackets represent the error of the deconvolution and the variation of the results from the repeated experiments. While we found that the fitting of the PLE peaks gives accurate results (see Figure S6 for the spectra), because of the inaccuracy of the method for calculation of the crystal field strength, only the trend should be taken into account.

**Table 2. PLE Maxima and Crystal Field Strength at Different $T_A$'s[a]**

| $T_A$ (°C) | $^4T_2$ (nm) | $^4T_1$ (nm) | 10Dq/B |
|---|---|---|---|
| 200 | 406 | 566 | 25.4988(250) |
| 400 | 405 | 566 | 25.2068(500) |
| 600 | 404 | 566 | 24.9177(150) |
| 800 | 404 | 562 | 25.7567(85) |
| 1100 | 403 | 557 | 26.5472(50) |

[a]The calculated values are close to the 27-28 10Dq/B value of ZGO:Cr, and a significant decrease can be observed at $T_A$ = 400 and 600 °C.

The reduction of the crystal field strength at a low $T_A$, the appearance of a new infrared peak, and the calculated larger core volume suggest that the crystal field strength is significantly reduced in the vicinity of some Cr defects in the core after annealing them between 200−600 °C. The emission from these Cr defects here is also coming from the $^4T_2$−$^4A_2$ transition, at least, partially, and as a result, the PL intensity of the $^2E$−$^4A_2$ transition reduces.

The thickness of the near-surface layer seems to depend on $T_A$ and crystal size. The depression of melting temperature at the nanoscale is well known, and the formation of a quasi-melted pseudocrystalline surface on NPs is also proven in experiments.[42] The pseudocrystalline near-surface layer increases with elevated temperatures at a constant particle size, and it decreases when particles grow. We believe that the formation of the pseudocrystalline layer, which enables crystal reorientation around Cr defects, already has a highly perturbed environment which reduces the crystal field strength. Simultaneously, surface reconstruction and crystal growth increase the symmetry around Cr defects, when possible, i.e., in the absence of the $SiO_2$ shell. For $T_A$ > 800 °C, the diffusion of the ions enables faster reconstruction by decreasing the concentration of the antisite-vacancy complexes responsible for the N2 centers and crystal growth, even in the presence of a porous $SiO_2$ layer. At $T_A$ = 1100 °C, the stability of the ZGO crystal reduces, possibly due to the phase separation reported at this temperature.[30]

Briefly, we conclude the following from our study. The N2 defect has higher emission intensity than the R1 defect and its concentration decreases for $T_A$ > 800 °C. This reduces the emission upon continuous UV−vis excitation. The R1 defects contribute to the exciton relaxation pathways upon X-ray exposure which makes XEOL intensity less sensitive to the N2 center's concentration. Previously, the LLP was associated with the N2 optical center, and many studies reported a connection between the N2 concentration and the LLP properties. In the case of an energy transfer between R1 and N2 centers, it is hard to prove such a correlation. However, we do not see a strong correlation between the contribution of the N2 center to the emission spectra and the measured LLP time, rather a complex correlation between trap states' concentration and Cr defect type, and the LLP decay. Deep traps, with levels near the conduction band minimum or one of the Cr defect's excited states, are needed for LLP. In our experiments, the presence of these traps is independent of the N2 center's concentration. However, it was found that a nearly perfect crystalline environment is needed for LLP, and the higher LLP intensity at the early stage of the relaxation for samples with 1100 °C annealing temperature suggests that the different ground state position of the newly formed N3 defects or the new trap states created by the enhanced diffusion of Zn affect the exciton annihilation processes.

## CONCLUSIONS

We applied a solvothermal synthesis process with a low energy cost for synthesizing small chromium-doped ZGO NPs. The crystallinity, size, and defects hosted by the nanoparticles can be engineered by post-annealing. We find that the optimum annealing temperature of chromium-doped ZGO NPs depends on the target characteristics of the optical spectrum. A short, 2 h annealing of the as-prepared ZGO NPs at 800 °C increases the emission intensity by an order of magnitude, and a higher annealing temperature reduces the photoluminescence intensity upon ultraviolet illumination, but the intensity remains substantial upon X-ray exposure. The photoluminescence emission upon X-ray excitation is associated by phonons and becomes efficient through the R1 defect.

We associate the bright LLP upon UV illumination by annealing of as-prepared samples at elevated temperatures with the creation of new traps that can trap excitons for LLP, and its correlation with the concentration of N2 optical centers—suggested previously in the literature—is not confirmed by our studies. We showed an efficient energy transfer between the R1 and R2 defects that makes the N2 center dominant regardless of the N2 center's concentration at room temperature. The exciton transfer from the trap states seems to be efficient toward the R1 defect, and LLP depends on the types and concentrations of the trap states.



https://doi.org/10.1021/acsanm.2c01156
ACS Appl. Nano Mater. 2022, 5, 8950−8961

We introduced a method to quantify the optical emission upon X-ray exposure by means of a home-built setup. We find that IR700 dye molecules can be efficiently excited by the optimized chromium-doped ZGO NPs to activate photodynamic therapy mediated by IR700 dye molecules. Further optimization of X-ray excitation optical luminescence may be envisioned by co-doping with other transition-metal ions which introduce new traps to elongate LLP. Other dopants in ZGO NPs may be employed to fine-tune the optical spectrum upon X-ray exposure for certain applications too as the solvothermal synthesis method can be principally extended to other transition-metal ions.

## METHODS

**Synthesis Procedures.** Chromium-doped $ZnGa_2O_4$ (ZGO:Cr) samples were prepared by a hydrothermal technique based on our previous method.[24] Briefly, 1 mL of $Zn(NO_3)_2$, $Ga(NO_3)_3$, and $Cr(NO_3)_3$ solutions from 2 mol/L $Zn(NO_3)_2{\cdot}6H_2O$ (99.9%), 2 mol/L $Ga(NO_3)_3{\cdot}H_2O$ (99.9%), and 4 mmol/L $Cr(NO_3)_3{\cdot}9H_2O$ (99%) (Merck (Sigma-Aldrich)), aqueous solutions, respectively, were mixed, and the total volume was adjusted to 15 mL with deionized (DI) water (Millipore type I). The mixture was stirred for 30 min. A 2 mL aliquot of ammonium hydroxide (32%, Avantor-VWR, a.r.) was added to the mixtures to achieve a pH of 9. After another 30 min of stirring, the precursors were sealed into a PTFE-lined autoclave (Berghof DAB 2) and annealed at 220 °C for 10 h (Berghof, DAH heating block, BTC-3000 Temperature Controller). The white precipitate obtained after the reaction was centrifuged out and washed with HCI−IPA (0.1 mol/L HCl and isopropyl alcohol (IPA) in a 1:10 ratio), after which it was dried at 60 °C.

For coating the samples with $SiO_2$ shell, we used Stöber silica synthesis with the ratio used by Zou.;[29] 50 mg of ZGO:Cr, 24 mL of EtOH, 0.1 mL of tetraethyl orthosilicate (TEOS), and 1.35 mL of (32%) $NH_3$. The mixture was stirred for 4 h and washed with DI water and ethanol (3 times each) after centrifugation; finally, the samples were dried at 60 °C.

Annealing was done on powder samples in crucibles or EPR quartz capillaries, or the samples were pressed into a pellet with the same amount (120 mg) with a 13 mm Specac press die and 2−2.5 tons. The same method was used except the total powder quantity was adjusted for 120 mg of ZGO:Cr content in the pellet. The concentration of the colloid ZGO:Cr solution before $SiO_2$ formation was 3 mg/mL. We set the same volume after the reaction and used the same volume of ZGO:Cr−$SiO_2$ solution (40 mL) for the pellets. Pellet before and after calcination was used for PL, and XEOL measurement as is. For XRD and EPR measurements, pellets were powdered in an alumina mortal. Powders were sonicated for 10 min in water before drop-casting for SEM analysis. Dynamic light scattering (DLS) was used to determine the size of the aggregates in the aqueous solution (see Figure S7). Annealing and subsequent measurements were performed on powdered samples, without pellet formation as well. For PL and XEOL, the same amount of sample was used, and for EPR and XRD measurement, the appropriate sample tube with optimized quantity was used.

Pellets were annealed in a ~20 × 20 × 30 $cm^3$ furnace or a tube furnace ($l$ = 30 cm, $d$ = 5 cm). All of the treatments had an annealing step at 350 °C, except for the ZGO:Cr-200 and ZGO:Cr−$SiO_2$-200. The temperature was increased by 3 °C/min. Cooling time was 4−6 h depending on $T_A$ when the larger furnace was used. Samples annealed in the tube furnace were removed after the annealing reaction and measured 30 min later. We compared the samples annealed in the two furnaces with similar conditions and saw no differences in the measured data. The tube furnace was then used for annealing-time optimization and repetitions for EPR and PL measurements.

X-ray powder diffraction (XRPD) data were measured on a Huber G670 Guinier Imaging Plate Camera using Cu K$\alpha_1$ radiation ($\alpha$ = 1.54056 Å) from a focusing Johannson monochromator. During the measurements, the samples were held in glass capillaries of 0.5 mm diameter and 0.01 mm wall thickness at room temperature. The Rietveld refinements were performed using the Topas Academic (by Alan A. Coleho, http://www.topas-academic.net/) program.

X-ray excited optical luminescence (XEOL) measurements with nonmonochromatized X-ray radiation were performed using a conventional sealed tube X-ray source and an Ocean Optics QE Pro-FL spectrometer (wavelength range: 350−1100 nm), optical resolution (HC1 grating, 200 $\mu$m slit): ~6.4 nm. For ZPL identification an Ocean Optics QE5000 spectrometer with 0.25 nm resolution was used. The unfiltered, nonmonochromatized X-ray radiation from the X-ray source contained both the characteristic radiation of the Mo anode (Mo K$\alpha$ at 17.5 keV, Mo K$\beta$ at 19.6 keV) and continuous bremsstrahlung radiation up to 50 keV energy. The Be window of the source and the 90 mm air-path from the source to the sample effectively absorbed the radiation below 3 keV photon energy. The sample was placed on a sample holder with holes of 8.5 mm in diameter, and it is positioned at a 45° angle with respect to the X-ray excitation beam. The substrate was irradiated with a spot size of 80 $mm^2$. The emitted light from this area was collected by a QP600-025-UV-BX optical fiber (NA 0.22) placed at 30 mm from the sample surface with a 90° angle with respect to the excitation X-ray beam. The optical fiber was connected to the Ocean Optics QE Pro-FL spectrometer. Long-lasting photoluminescence (LLP) was recorded with a TAPO C210 camera in the visible range and in the infrared range after UV exposure. In the case of X-ray excitation, only the visible mode was used, and LLP was calculated from the previous measurements.

The decay curve of LLP was measured with the Ocean Optics spectrometer with 100 ms integration time and 100 ms delay time. Absolute irradiance and dose were calculated from the spectra, or the decay curve recorded by the spectrometer using the calibration curve and measurement protocol provided by the manufacturer. Calibration was validated by measuring the emission intensity of 520, 637, and 785 nm laser beams with known beam size. Output power was measured with a calibrated powermeter (S121C photodiode and PM100D powermeter, Thorlabs).

The equation used for the calibration is

$$I_P = \frac{(S_P - D_P)^* C_P}{(T^* A^* dL_P)}$$

where $I_p$ is the power density (W/$cm^2$), $S_p$ is the total counts of the emitted light from the sample, $D_p$ is the dark counts from the same area when the excitation was switched off, $C_P$ is the calibration constant (J/counts), $T$ is the integration time (s), $A$ is the collection area ($cm^2$), and $dL_p$ is the wavelength spread resolution (wavelength/pixel in dimensionless unit).

In the case of continuous X-ray excitation, the output power density is constant, and the time required for the 2 J/$cm^2$ dose was calculated from the measured power density considering only the overlapping area with the absorption spectrum of IR700 as indicated in Figure 2c. In the case of the LLP, the power density decreases over time. The beginning of the decay curve can be fitted with multiple exponentials, while the rest can be fitted by a single exponential (see Figure 2b). We used only the slowly decaying part of the LLP to calculate the required dose for the IR700-mAb activation. The fitted decay curve was integrated to find the integration time required for reaching the total excitation power density of 2 J/$cm^2$.

Photoluminescence spectroscopy (PL) and photoluminescence excitation spectroscopy (PLE) measurements were performed on a Horiba Jobin-Yvon NanoLog FL3-2iHR spectrophotometer equipped with a 450 W Xenon lamp, an iHR-320 grating spectrometer, and an R928P photomultiplier tube. In the case of colloids, the measurements were carried out in a 10 mm quartz cuvette (Hellma 110-QS). The PLE was recorded at 695 nm emission wavelength at a slit size of 10 nm.

For the 250 nm UV illumination, a 400 W black light tube was used.

We studied X-band electron paramagnetic resonance (EPR at 0.35 T and 9.4 GHz) in a commercial spectrometer (Magnettech


https://doi.org/10.1021/acsanm.2c01156
ACS Appl. Nano Mater. 2022, 5, 8950−8961

MiniScope MS-400) equipped with a TE102 rectangular cavity. Continuous flow of dry nitrogen gas was applied to avoid moisture and droplet formation in the cavity. Samples were placed in high-quality, defect-free quartz ampoules (Wilmad LabGlass). Special care was taken to employ a low microwave excitation power (2 mW) with low magnetic field (1.0−2.5 G) modulation to avoid any distortion to the EPR line shapes. The measurements were carried out at room temperature, so the charge state of the defects was determined in thermal equilibrium under ambient conditions. 50.0 mg of sample was used for the measurement.

Scanning electron microscopy (SEM) images and energy-dispersive spectroscopic (EDS) data were recorded by a TESCAN MIRA3 electron microscope equipped with an Element EDS system. The SEM images were taken by applying In-Beam Secondary Electron (SE) mode. For the measurements, the NPs were diluted in ethanol and drop-cast on Si surface or on highly ordered pyrolytic graphite (HOPG) substrate.

Raman measurements were carried out with a Renishaw InVia confocal Raman microscope and a 2 W continuous 532 nm laser source at 1% intensity, the power at the sample is estimated to be around 20 mW.

Low-temperature photoluminescence (LTPL) measurements were carried out in our home-built confocal setup with the sample placed in a cryostat (Montana Cryostation s50). The 520 nm laser excitation (home-built, based on PLT5 520B laser diode) was focused on the sample by the objective (ZEISS EC Epiplan-Neofluar 100×/0.90) at 0.5 mW power before the objective. A PL spectrometer (Ocean Optics QE5000 with 0.25 nm resolution) was applied to record the PL spectra. A 550 nm long-pass optical filter (Thorlabs FEL550) was used to exclude the radiation from the laser source.

## ■ ASSOCIATED CONTENT

### Supporting Information

The Supporting Information is available free of charge at https://pubs.acs.org/doi/10.1021/acsanm.2c01156.

Additional experimental details and results including a table with $t_1$ and $t_2$ lifetimes; SEM images; Raman spectra; PL spectra; XEOL spectra; PLE spectra, and particle size distribution measured by DLS (PDF)

## ■ AUTHOR INFORMATION


### Corresponding Author

**Adam Gali** − *Wigner Research Centre for Physics, Institute for Solid State Physics and Optics, H-1525 Budapest, Hungary; Department of Atomic Physics, Institute of Physics, Budapest University of Technology and Economics, H-1111 Budapest, Hungary;* orcid.org/0000-0002-3339-5470; Email: gali.adam@wigner.hu

### Authors

**Mátyás M. Rudolf** − *Department of Physical Chemistry and Materials Science, Faculty of Chemical Technology and Biotechnology, Budapest University of Technology and Economics, H-1111 Budapest, Hungary; Wigner Research Centre for Physics, Institute for Solid State Physics and Optics, H-1525 Budapest, Hungary;* orcid.org/0000-0001-5435-3694

**Gábor Bortel** − *Wigner Research Centre for Physics, Institute for Solid State Physics and Optics, H-1525 Budapest, Hungary;* orcid.org/0000-0002-6290-4377

**Bence G. Márkus** − *Wigner Research Centre for Physics, Institute for Solid State Physics and Optics, H-1525 Budapest, Hungary; Stavropoulos Center for Complex Quantum Matter, Department of Physics, University of Notre Dame, South Bend, Indiana 46556, United States*

**Nikoletta Jegenyes** − *Wigner Research Centre for Physics, Institute for Solid State Physics and Optics, H-1525 Budapest, Hungary;* orcid.org/0000-0003-1561-4884

**Vladimir Verkhovlyuk** − *Wigner Research Centre for Physics, Institute for Solid State Physics and Optics, H-1525 Budapest, Hungary;* orcid.org/0000-0003-0967-1364

**Katalin Kamarás** − *Wigner Research Centre for Physics, Institute for Solid State Physics and Optics, H-1525 Budapest, Hungary*

**Ferenc Simon** − *Wigner Research Centre for Physics, Institute for Solid State Physics and Optics, H-1525 Budapest, Hungary; Department of Physics, Institute of Physics, Budapest University of Technology and Economics, H-1111 Budapest, Hungary;* orcid.org/0000-0001-9822-4309

**David Beke** − *Wigner Research Centre for Physics, Institute for Solid State Physics and Optics, H-1525 Budapest, Hungary; Department of Atomic Physics, Institute of Physics, Budapest University of Technology and Economics, H-1111 Budapest, Hungary;* orcid.org/0000-0001-6046-8164

Complete contact information is available at: https://pubs.acs.org/10.1021/acsanm.2c01156


### Author Contributions

M.M.R. and D.B. prepared the samples and analyzed them with various experimental techniques. G.B. analyzed the samples by X-ray diffraction. B.G.M. and F.S. contributed to the electron paramagnetic resonance measurements and analysis. N.J. carried out the scanning electron microscopy measurements and contributed to the analysis. V.V. carried out low-temperature photoluminescence spectroscopy and analysis, whereas K.K. contributed to the analysis of the photoluminescence spectrum. D.B. and A.G. conceived the research and managed the work. D.B. wrote the manuscript together with A.G., and all of the authors contributed to the writing of the final version of the manuscript.


### Funding

National Research, Development and Innovation Fund (NKFIH) and Hungarian Academy of Sciences.


### Notes

The authors declare no competing financial interest.

The Hungarian research infrastructure for the studies at the Wigner Research Centre for Physics was provided by the Hungarian Academy of Sciences.

## ■ ACKNOWLEDGMENTS


This study was supported by the János Bolyai Scholarship of the Hungarian Academy of Sciences, UNKP-20 New National Excellence program, project no. TKP2021-NVA-04 provided by the Ministry of Innovation and Technology of Hungary from the National Research, Development and Innovation Fund (NKFIH), financed under the TKP2021-NVA funding scheme, the Quantum Information National Laboratory sponsored by the Ministry for Innovation and Technology of Hungary via NKFIH. This research was supported by Grant No. VEKOP-2.3.3-15-2016-00002 of the European Structural and Investment Funds. B.G.M. and F.S. acknowledge the support of the NKFIH Grant No. 137852. The research reported in this paper and carried out at BME has been supported by the NKFIH Fund (TKP2021) based on the charter of bolster issued by the NKFIH Office under the auspices of the Ministry for Innovation and Technology.

## REFERENCES


(1) Sharma, S. K.; Bessiere, A.; Gourier, D.; Binet, L.; Viana, B.; Basavaraju, N.; Priolkar, K.; Maldiney, T.; Scherman, D.; Richard, C. Persistent Luminescence in $ZnGa_2O_4$:Cr: An Outstanding Biomarker for In-Vivo Imaging. In *Proc. SPIE 8982, Optical Components and Materials XI*, 2014; p 898215.

(2) Bessière, A.; Jacquart, S.; Priolkar, K.; Lecointre, A.; Viana, B.; Gourier, D. $ZnGa_2O_4Cr^{3+}$: A New Red Long-Lasting Phosphor with High Brightness. *Opt. Express* **2011**, *19*, 10131−10137.

(3) da Silva, M. N.; de Carvalho, J. M.; de Abreu Fantini, M. C.; Chiavacci, L. A.; Bourgaux, C. Nanosized $ZnGa_2O_4$:$Cr^{3+}$ Spinels as Highly Luminescent Materials for Bioimaging. *ACS Appl. Nano Mater.* **2019**, *2*, 6918−6927.

(4) Liu, J.; Lécuyer, T.; Seguin, J.; Mignet, N.; Scherman, D.; Viana, B.; Richard, C. Imaging and Therapeutic Applications of Persistent Luminescence Nanomaterials. *Adv. Drug Delivery Rev.* **2019**, *138*, 193−210.

(5) Cha, J. H.; Choi, H. W. Luminescence Characteristics of $ZnGa_2O_4$:$Mn^{2+}$,$Cr^{3+}$ Phosphor and Thick Film. *Trans. Electr. Electron. Mater.* **2011**, *12*, 11−15.

(6) dos S Rezende, M. V.; Montes, P. J. R.; Andrade, A. B.; Macedo, Z. S.; Valerio, M. E. G. Mechanism of X-Ray Excited Optical Luminescence (XEOL) in Europium Doped $BaAl_2O_4$ Phosphor. *Phys. Chem. Chem. Phys.* **2016**, *18*, 17646−17654.

(7) Karthik H G, S.; Menon, S. G.; Hebbar N, D.; Choudhari, K. S.; Santhosh, C.; Kulkarni, S. D. Effect of Zn Substitution in $Cr^{3+}$ Doped $MgAl_2O_4$ Mixed Spinel Nanoparticles on Red/NIR Emission Properties. *Mater. Res. Bull.* **2019**, *111*, 294−300.

(8) Gu, Z.; Liu, F.; Li, X.; Howe, J.; Xu, J.; Zhao, Y.; Pan, Z. Red, Green, and Blue Luminescence from $ZnGa_2O_4$ Nanowire Arrays. *J. Phys. Chem. Lett.* **2010**, *1*, 354−357.

(9) Kobayashi, H.; Choyke, P. L. Near-Infrared Photoimmunotherapy of Cancer. *Acc. Chem. Res.* **2019**, *52*, 2332−2339.

(10) Mitsunaga, M.; Ogawa, M.; Kosaka, N.; Rosenblum, L. T.; Choyke, P. L.; Kobayashi, H. Cancer Cell−Selective in Vivo near Infrared Photoimmunotherapy Targeting Specific Membrane Molecules. *Nat. Med.* **2011**, *17*, 1685−1691.

(11) Xue, Z.; Li, X.; Li, Y.; Jiang, M.; Liu, H.; Zeng, S.; Hao, J. X-ray-Activated near-Infrared Persistent Luminescent Probe for Deep-Tissue and Renewable in Vivo Bioimaging. *ACS Appl. Mater. Interfaces* **2017**, *9*, 22132−22142.

(12) Kobayashi, T.; Harada, K.; Kumagai, Y.; Oba, F.; Matsushita, Y. I. Native Point Defects and Carbon Clusters in 4H-SiC: A Hybrid Functional Study. *J. Appl. Phys.* **2019**, *125*, No. 125701.

(13) Basavaraju, N.; Priolkar, K. R.; Gourier, D.; Sharma, S. K.; Bessière, A.; Viana, B. The Importance of Inversion Disorder in the Visible Light Induced Persistent Luminescence in $Cr^{3+}$ Doped $AB_2O_4$ (A = Zn or Mg and B = Ga or Al). *Phys. Chem. Chem. Phys.* **2015**, *17*, 1790−1799.

(14) Can, M. M.; Jaffari, G. H.; Aksoy, S.; Shah, S. I.; Firat, T. Synthesis and Characterization of $ZnGa_2O_4$ Particles Prepared by Solid State Reaction. *J. Alloys Compd.* **2013**, *549*, 303−307.

(15) Castaing, V.; Sontakke, A. D.; Fernández-Carrión, A. J.; Touati, N.; Binet, L.; Allix, M.; Gourier, D.; Viana, B. Persistent Luminescence of $ZnGa_2O_4$:$Cr^{3+}$ Transparent Glass Ceramics: Effects of Excitation Wavelength and Excitation Power. *Eur. J. Inorg. Chem.* **2017**, *2017*, 5114−5120.

(16) Hussen, M. K.; Dejene, F. B. Effect of $Cr^{3+}$ Doping on Structural and Optical Property of $ZnGa_2O_4$ Synthesized by Sol Gel Method. *Optik* **2019**, *181*, 514−523.

(17) Yu, M.; Lin, J.; Zhou, Y.; Wang, S. Citrate−Gel Synthesis and Luminescent Properties of $ZnGa_2O_4$ Doped with $Mn^{2+}$ and $Eu^{3+}$. *Mater. Lett.* **2002**, *56*, 1007−1013.

(18) Srivastava, B. B.; Kuang, A.; Mao, Y. Persistent Luminescent Sub-10 Nm Cr Doped $ZnGa_2O_4$ Nanoparticles by a Biphasic Synthesis Route. *Chem. Commun.* **2015**, *51*, 7372−7375.

(19) Luan, T.; Liu, J.; Yuan, X.; Li, J. G. Controlled Hydrothermal Synthesis and Photoluminescence of Nanocrystalline $ZnGa_2O_4$:$Cr^{3+}$ Monospheres. *Nanoscale Res. Lett.* **2017**, *12*, No. 219.

(20) Wei, X.; Huang, X.; Zeng, Y.; Jing, L.; Tang, W.; Li, X.; Ning, H.; Sun, X.; Yi, Y.; Gao, M. Longer and Stronger: Improving Persistent Luminescence in Size-Tuned Zinc Gallate Nanoparticles by Alcohol-Mediated Chromium Doping. *ACS Nano* **2020**, *14*, 12113−12124.

(21) Li, Z.; Zhang, Y.; Wu, X.; Huang, L.; Li, D.; Fan, W.; Han, G. Direct Aqueous-Phase Synthesis of Sub-10 Nm "Luminous Pearls" with Enhanced in Vivo Renewable near-Infrared Persistent Luminescence. *J. Am. Chem. Soc.* **2015**, *137*, 5304−5307.

(22) Ueda, J.; Back, M.; Brik, M. G.; Zhuang, Y.; Grinberg, M.; Tanabe, S. Ratiometric Optical Thermometry Using Deep Red Luminescence from $^4T_2$ and $^2E$ States of $Cr^{3+}$ in $ZnGa_2O_4$ Host. *Opt. Mater.* **2018**, *85*, 510−516.

(23) Zhang, W.; Zhang, J.; Wan, H.; Chen, Z.; Wang, T. Photoluminescence Properties Influenced by Calcining Condition and Doping Concentration of Nano-Sized $ZnGa_2O_4$: $Cr^{3+}$. *Mater. Sci. Forum* **2009**, *610−613*, 616−620.

(24) Beke, D.; Nardi, M. V.; Bortel, G.; Timpel, M.; Czigány, Z.; Pasquali, L.; Chiappini, A.; Bais, G.; Rudolf, M.; Zalka, D.; Bigi, F.; Rossi, F.; Bencs, L.; Pekker, A.; Márkus, B. G.; Salviati, G.; Saddow, S. E.; Kamarás, K.; Simon, F.; Gali, A. Enhancement of X-Ray-Excited Red Luminescence of Chromium-Doped Zinc Gallate via Ultrasmall Silicon Carbide Nanocrystals. *Chem. Mater.* **2021**, *33*, 2457−2465.

(25) Basavaraju, N.; Priolkar, K. R.; Bessière, A.; Sharma, S. K.; Gourier, D.; Binet, L.; Viana, B.; Emura, S. Controlling Disorder in the $ZnGa_2O_4$:$Cr^{3+}$ Persistent Phosphor by $Mg^{2+}$ Substitution. *Phys. Chem. Chem. Phys.* **2017**, *19*, 1369−1377.

(26) Zhuang, Y.; Ueda, J.; Tanabe, S. Enhancement of Red Persistent Luminescence in Cr $^{3+}$ Doped $ZnGa_2O_4$ Phosphors by $Bi_2O_3$ Codoping. *Appl. Phys. Express* **2013**, *6*, No. 052602.

(27) Glais, E.; Pellerin, M.; Castaing, V.; Alloyeau, D.; Touati, N.; Viana, B.; Chanéac, C. Luminescence Properties of $ZnGa_2O_4$:$Cr^{3+}$,$Bi^{3+}$ Nanophosphors for Thermometry Applications. *RSC Adv.* **2018**, *8*, 41767−41774.

(28) Wani, S.; Sofi, H. S.; Sheikh, F. A.; Shivashankar, S. A.; Majeed, S. $ZnGa_2O_4$ Nanophosphors: Rapid Synthesis, Characterization and Luminescence Properties. *Mater. Sci. Res. India* **2017**, *14*, 116−122.

(29) Zou, R.; Huang, J.; Shi, J.; Huang, L.; Zhang, X.; Wong, K. L.; Zhang, H.; Jin, D.; Wang, J.; Su, Q. Silica Shell-Assisted Synthetic Route for Mono-Disperse Persistent Nanophosphors with Enhanced in Vivo Recharged near-Infrared Persistent Luminescence. *Nano Res.* **2017**, *10*, 2070−2082.

(30) Hussen, M. K.; Dejene, F. B. Influence of Annealing Temperature on Material Properties of Red Emitting $ZnGa_2O_4$: $Cr^{3+}$ Nanostructures. *J. Sol-Gel Sci. Technol.* **2018**, *88*, 454−464.

(31) Pan, Z.; Lu, Y. Y.; Liu, F. Sunlight-Activated Long-Persistent Luminescence in the near-Infrared from $Cr^{3+}$-Doped Zinc Gallogermanates. *Nat. Mater.* **2012**, *11*, 58−63.

(32) Nakajima, T.; Sato, K.; Hanaoka, H.; Watanabe, R.; Harada, T.; Choyke, P. L.; Kobayashi, H. The Effects of Conjugate and Light Dose on Photo-Immunotherapy Induced Cytotoxicity. *BMC Cancer* **2014**, *14*, No. 389.

(33) Errandonea, D.; Kumar, R. S.; Manjón, F. J.; Ursaki, V. V.; Rusu, E. V. Post-Spinel Transformations and Equation of State in $ZnGa_2O_4$: Determination at High Pressure by in Situ x-Ray Diffraction. *Phys. Rev. B* **2009**, *79*, No. 024103.

(34) Mitran, R. A.; Culita, D. C.; Atkinson, I. Thermal Stability Enhancement of Mesoporous SBA-15 Silica through Nanoconfinement of Ceria Nanoparticles. *Microporous Mesoporous Mater.* **2020**, *306*, No. 110484.

(35) van Gorkom, G. G. P.; Henning, J. C. M.; van Stapele, R. P. Optical Spectra of $Cr^{3+}$ Pairs in the Spinel $ZnGa_2O_4$. *Phys. Rev. B* **1973**, *8*, 955−973.

(36) Gourier, D.; Bessière, A.; Sharma, S. K.; Binet, L.; Viana, B.; Basavaraju, N.; Priolkar, K. R. Origin of the Visible Light Induced Persistent Luminescence of $Cr^{3+}$-Doped Zinc Gallate. *J. Phys. Chem. Solids* **2014**, *75*, 826−837.

(37) Bessière, A.; Sharma, S. K.; Basavaraju, N.; Priolkar, K. R.; Binet, L.; Viana, B.; Bos, A. J. J.; Maldiney, T.; Richard, C.; Scherman,




https://doi.org/10.1021/acsanm.2c01156
ACS Appl. Nano Mater. 2022, 5, 8950−8961

D.; Gourier, D. Storage of Visible Light for Long-Lasting Phosphorescence in Chromium-Doped Zinc Gallate. *Chem. Mater.* **2014**, *26*, 1365−1373.
(38) Basavaraju, N.; Priolkar, K. R.; Gourier, D.; Bessière, A.; Viana, B. Order and Disorder around $Cr^{3+}$ in Chromium Doped Persistent Luminescent $AB_2O_4$ Spinels. *Phys. Chem. Chem. Phys.* **2015**, *17*, 10993−10999.
(39) Tanaka, K.; Yamaguchi, I.; Hirao, K.; Soga, N. Optical Properties of Transparent Glass-Ceramics Containing $ZnGa_2O_4$:Cr Microcrystals. *Bull. Inst. Chem. Res. Kyoto Univ.* **1994**, *72*, 124−133.
(40) Brik, M. G.; Avram, N. M.; Avram, C. N. Comparative Crystal Field Calculations of the $Cr^{3+}$ Energy Level Schemes in $ZnAl_2S_4$ and $ZnGa_2O_4$. *J. Mater. Sci.: Mater. Electron.* **2009**, *20*, 30−32.
(41) Wang, W.-K.; Liu, K.-F.; Tsai, P.-C.; Xu, Y.-J.; Huang, S.-Y. Influence of Annealing Temperature on the Properties of $ZnGa_2O_4$ Thin Films by Magnetron Sputtering. *Coatings* **2019**, *9*, No. 859.
(42) Chang, J.; Johnson, E. Surface and Bulk Melting of Small Metal Clusters. *Philos. Mag.* **2005**, *85*, 3617−3627.





https://doi.org/10.1021/acsanm.2c01156
*ACS Appl. Nano Mater.* 2022, 5, 8950−8961